F1

Figure 2. Sunphotometer channel wavelengths (vertical lines with arrows) in relation to atmospheric spectra. The spectra of $\ln(1/T)$ were calculated for the transmission T of the direct solar beam at sea level using MODTRAN-3/Version 1.2 with a US Standard atmosphere, a spring-summer tropospheric aerosol model, and the sun at the zenith. Current center wavelengths of channel filters are 380.3, 448.3, 453.0, 499.4, 524.7, 605.4, 666.8, 711.8, 778.6, 864.4, 939.5, 1018.7, 1059.0, 1557.5 nm for AATS-14 and 380.1, 450.7, 525.3, 863.9, 941.4, 1020.7 nm for AATS-6. Filter full widths at half-maximum (FWHM) are 5 nm, except for the 448, 453, and 1558 nm channels, which have FWHM 0.94, 2.17, and 30 nm, respectively.
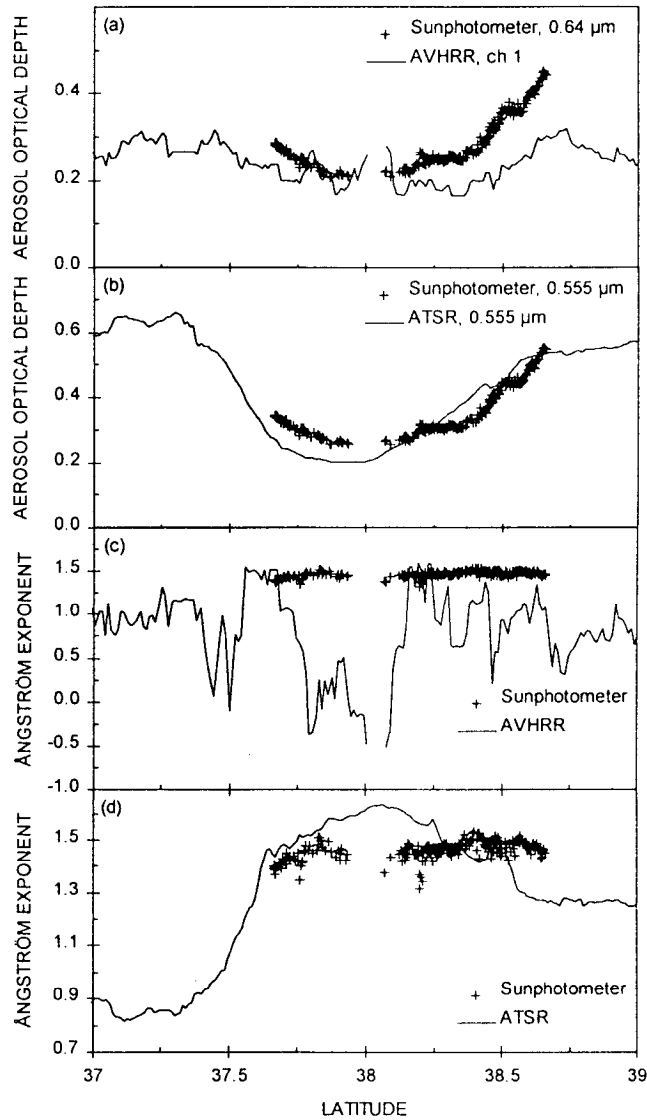
Figure 3. Latitude transects of aerosol optical depth and Ångström wavelength exponent as derived from the AATS-6 sunphotometer aboard the UW C-131A, the ATSR-2, and the AVHRR. (a) AVHRR retrieved aerosol optical depth for channel 1 (0.64 μm) and sunphotometer derived aerosol optical depth at 0.64 μm. (b) same as (a) but for ATSR-2 retrieved aerosol optical depth at 0.525 μm and sunphotometer derived aerosol optical depth at this wavelength; (c) Ångström wavelength exponent as derived from AVHRR and from sunphotometer data; (d) same as (c) but for Ångström wavelength exponent as derived from ATSR-2 and from sunphotometer data (Veefkind et al., 1999).
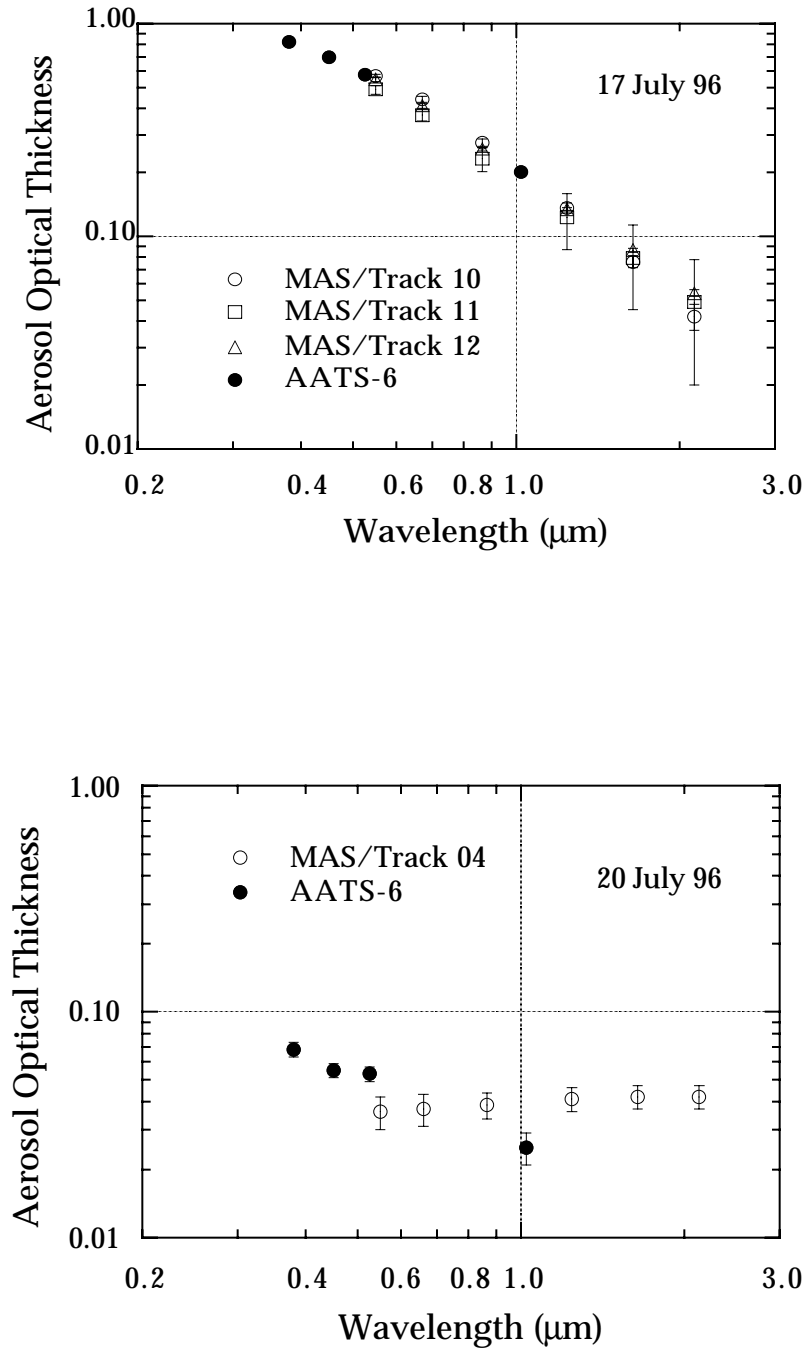
Figure 4. Aerosol optical thickness measured by sunphotometer (AATS-6) aboard the C-131A aircraft and derived from MAS data as a function of wavelength. Top frame: Comparison at 37.49°N/74.16°W around 1830UTC. Bottom frame: The sunphotometer data were acquired over point at 38.20°N/73.98°W at 1842UTC. The optical thicknesses derived from the MAS are averaged over a geographical area defined by points located at 38.17°N/74.0°W and 38.27°N/74.1°W; the time of the acquisition was around 1830UTC (Tanre et al., 1999).
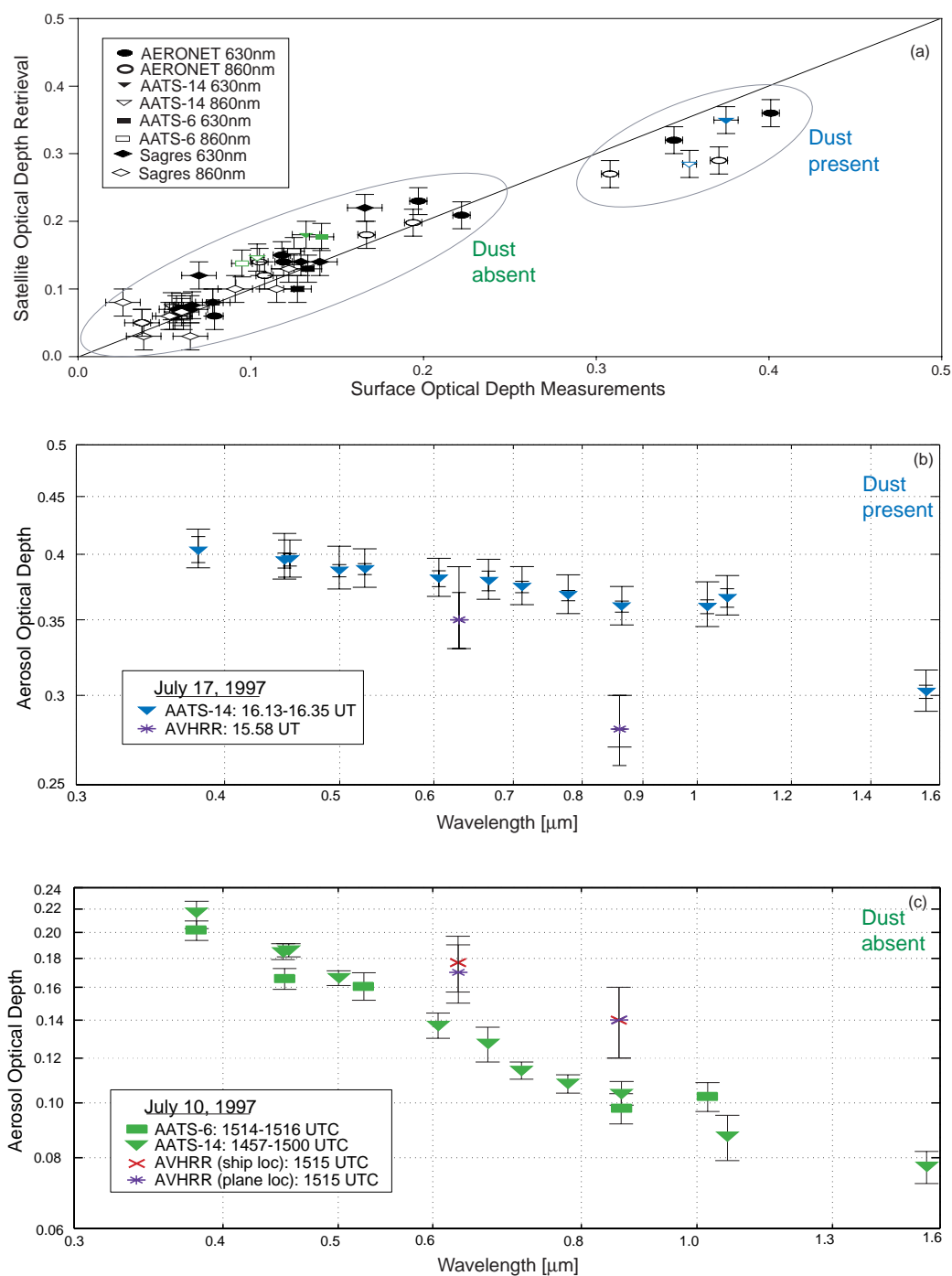
Figure 5. (a) Scatter diagram of aerosol optical depth retrieved from AVHRR on the NOAA-14 satellite versus that measured by various photometers at the surface (Durkee et al., 2000). (b) Comparison of aerosol optical depth spectra measured in ACE-2 by AATS-14 on the Pelican aircraft and AVHRR on the NOAA-14 Satellite, July 17, 1997. (Livingston et al., 2000; Schmid et al., 2000). (c) As in (b), for AATS-6 on the R/V Vodyanitskiy ship, AATS-14 on the Pelican aircraft, and AVHRR on the NOAA-14 Satellite, July 10, 1997.
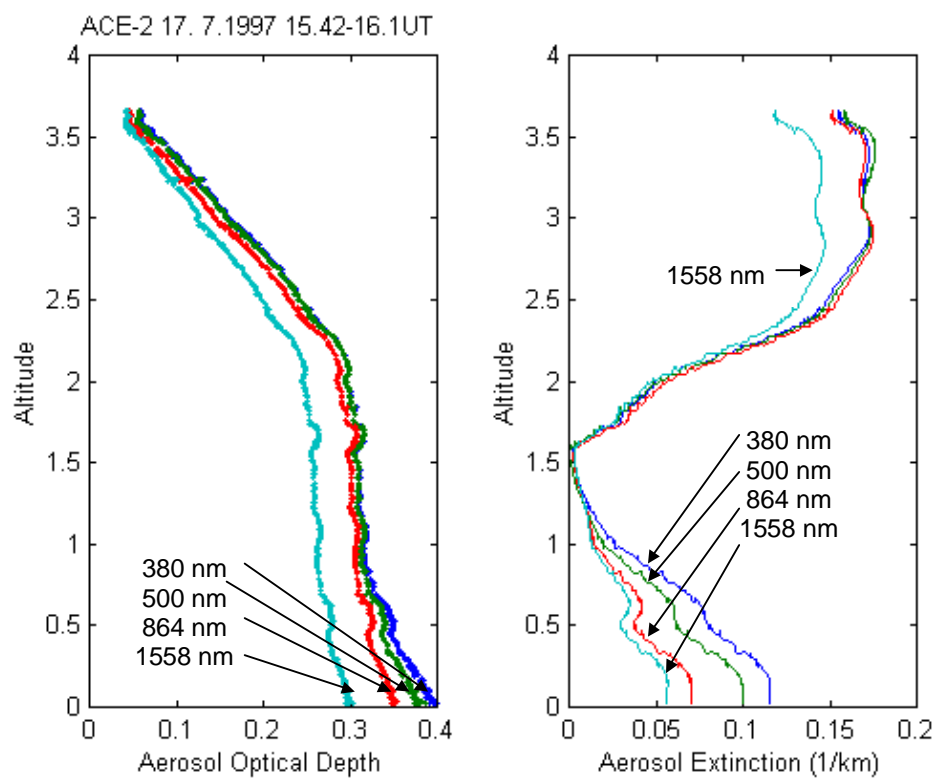
Figure 6. Left panel: Profiles of aerosol optical depth at four selected AATS-14 wavelengths (380, 500, 864 and 1558 nm) measured in ACE-2 south of the coast of Tenerife. Right panel: Aerosol extinction profiles derived by differentiating the profiles in the left panel. (Schmid et al., 2000b)
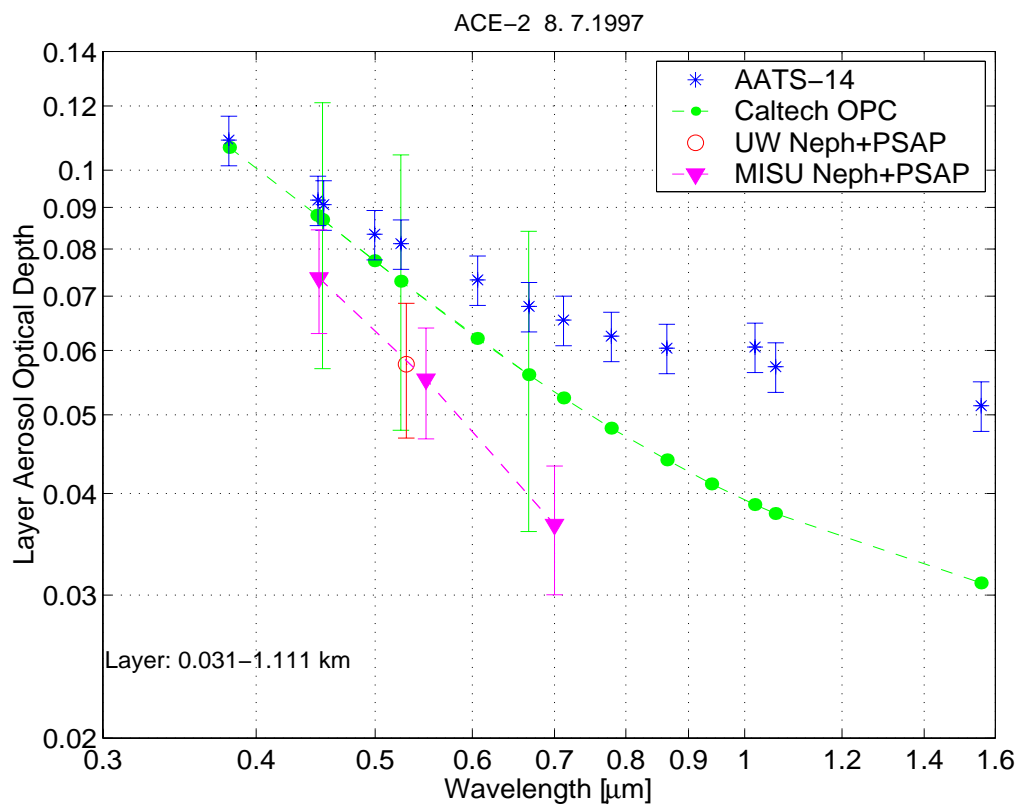
Figure 7. Comparison of aerosol optical depth spectra for the marine boundary layer (31-1111 m) during Pelican flight tf20 in ACE 2 on July 8, 1997 (Schmid et al., 2000).
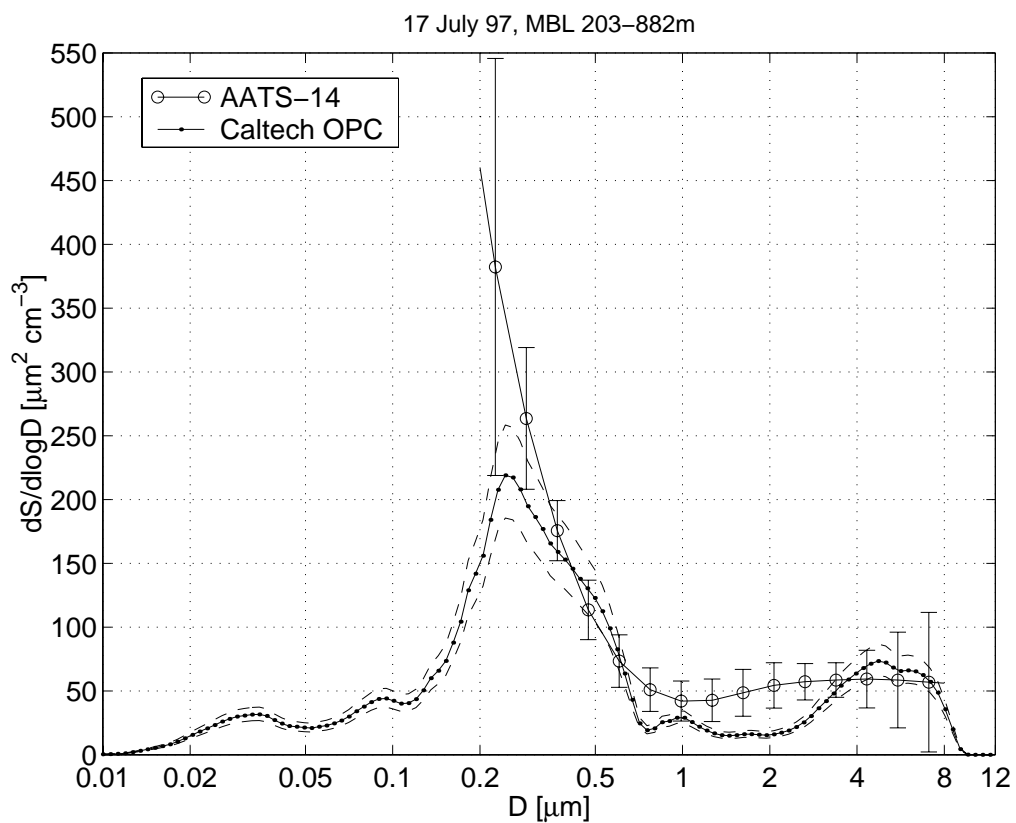
Figure 8. Comparison of marine boundary layer aerosol size distributions from in situ measurements and inverted from AATS-14 extinction spectra measured on Pelican flight tf15 in ACE 2 on July 17, 1997. Dashed lines indicate uncertainty of the in situ results (Schmid et al., 2000).
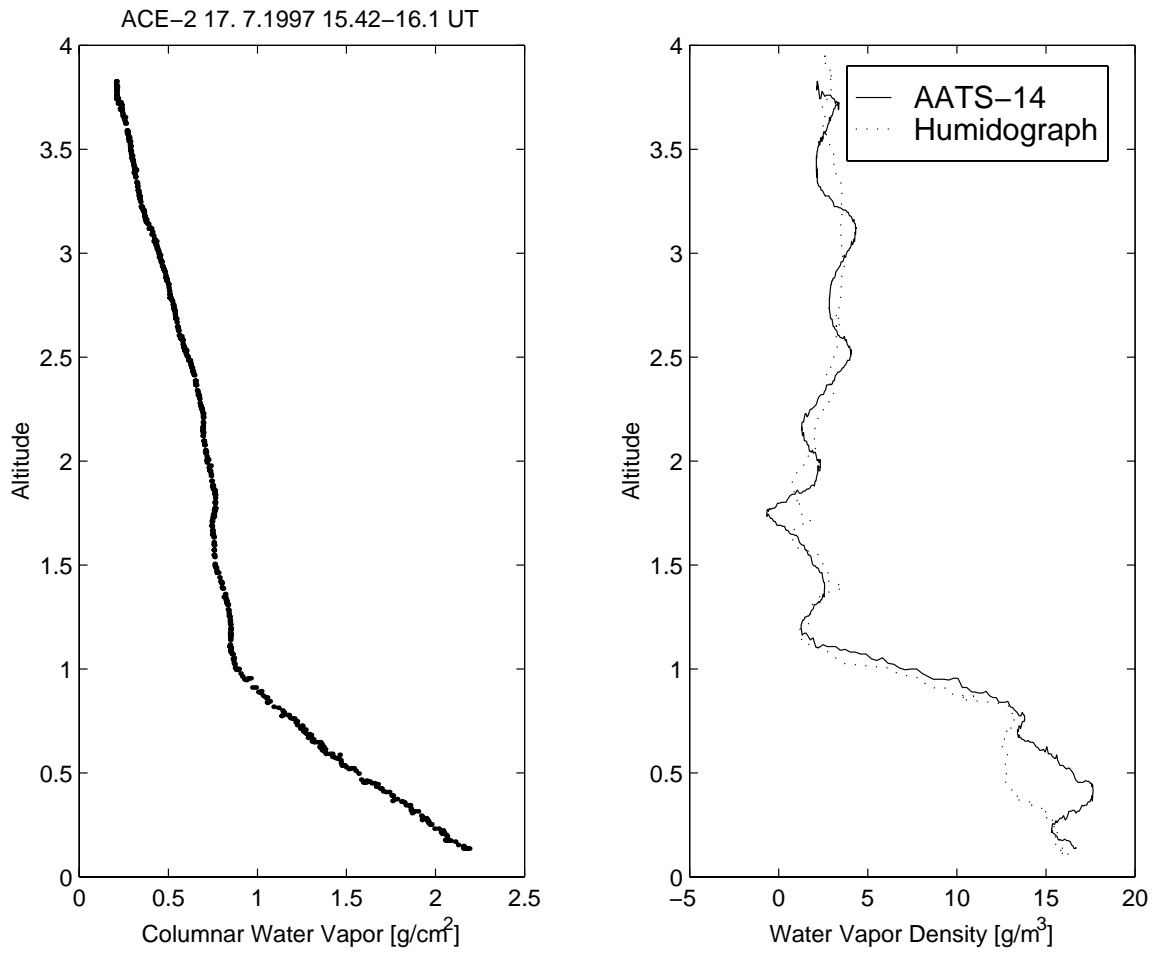
Figure 9. Left panel: Profile of the columnar water vapor above the Pelican aircraft measured in ACE-2 south of the coast of Tenerife. Right panel: Water vapor density derived by differentiating the profile in the left panel. Also shown for comparison is the profile obtained by combining readings of a humidograph and outside temperature on Pelican (humidograph data courtesy of S. Gasso, University of Washington). (Schmid et al., 2000)
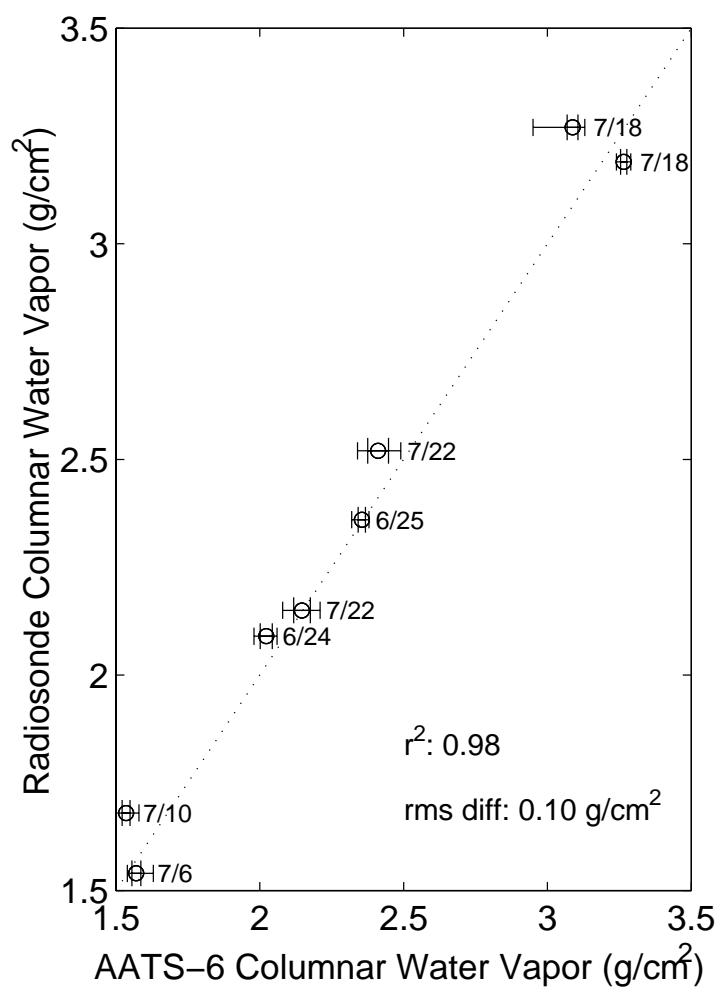
Figure 10. Scatter diagram of columnar water vapor calculated from radiosonde measurements and from AATS-6 measurements during ACE-2. Each AATS-6 data point represents the mean calculated over the time period spanned by the radiosonde measurements; horizontal bars show the corresponding standard deviation (wide ticks) and the range (narrow ticks) for that time period (Livingston et al., 2000).
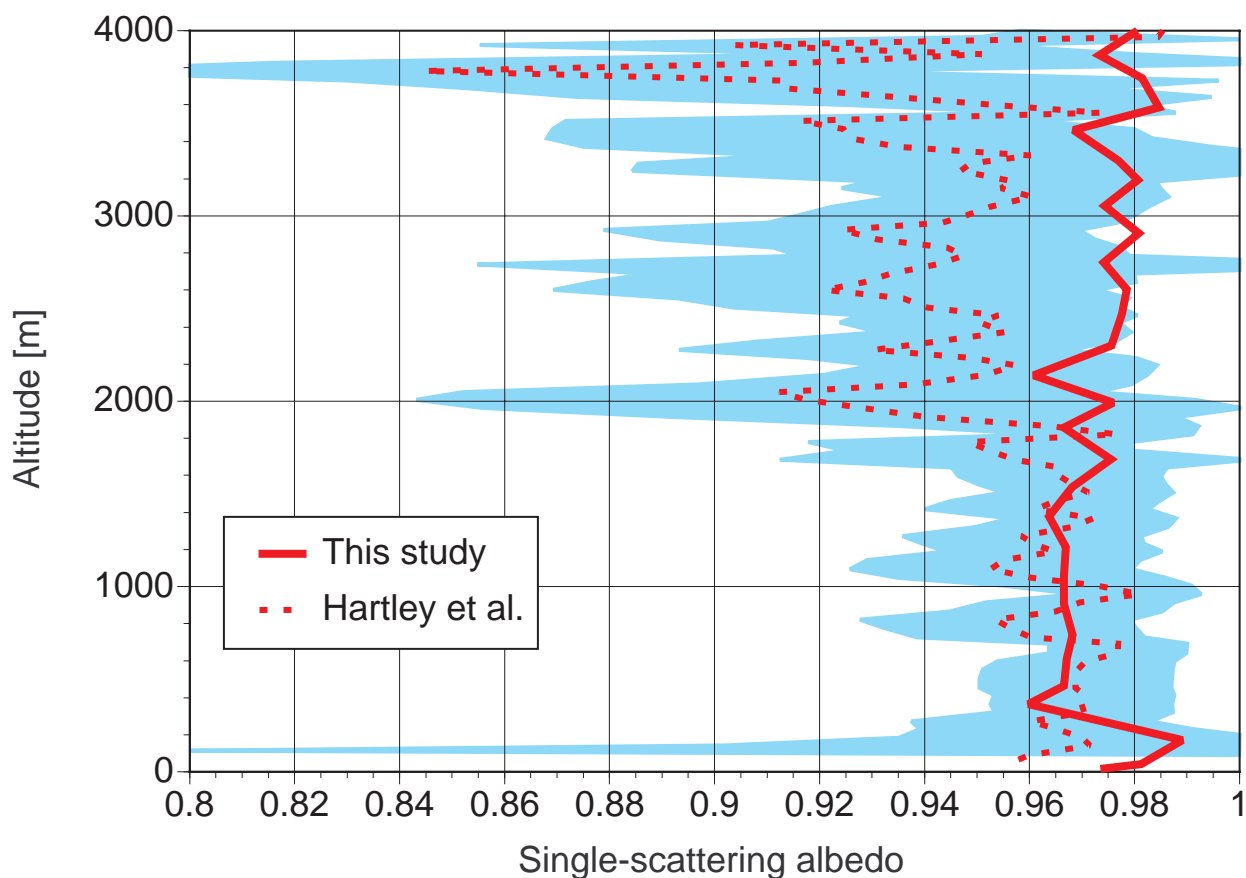
Figure 11. Aerosol single-scattering albedo profiles determined for TARFOX flight 1728 (July 17, 1996) by two techniques. Solid line: derived by Redemann et al. (2000b) using *in situ* particle size distributions and aerosol layer complex refractive index estimates from Redemann et al. (2000a) that produce best agreement among profiles of lidar backscatter, sunphotometer extinction, and relative size distribution. Values were used in the first band of the Fu-Liou radiative transfer model (0.2 μm < λ < 0.7 μm). Dashed line: derived by Hartley et al. (2000) at 450 nm by combining in situ scattering, absorption, and size distribution measurements. The gray-shaded area represents their uncertainty estimates based on one standard deviation plus instrumental error.
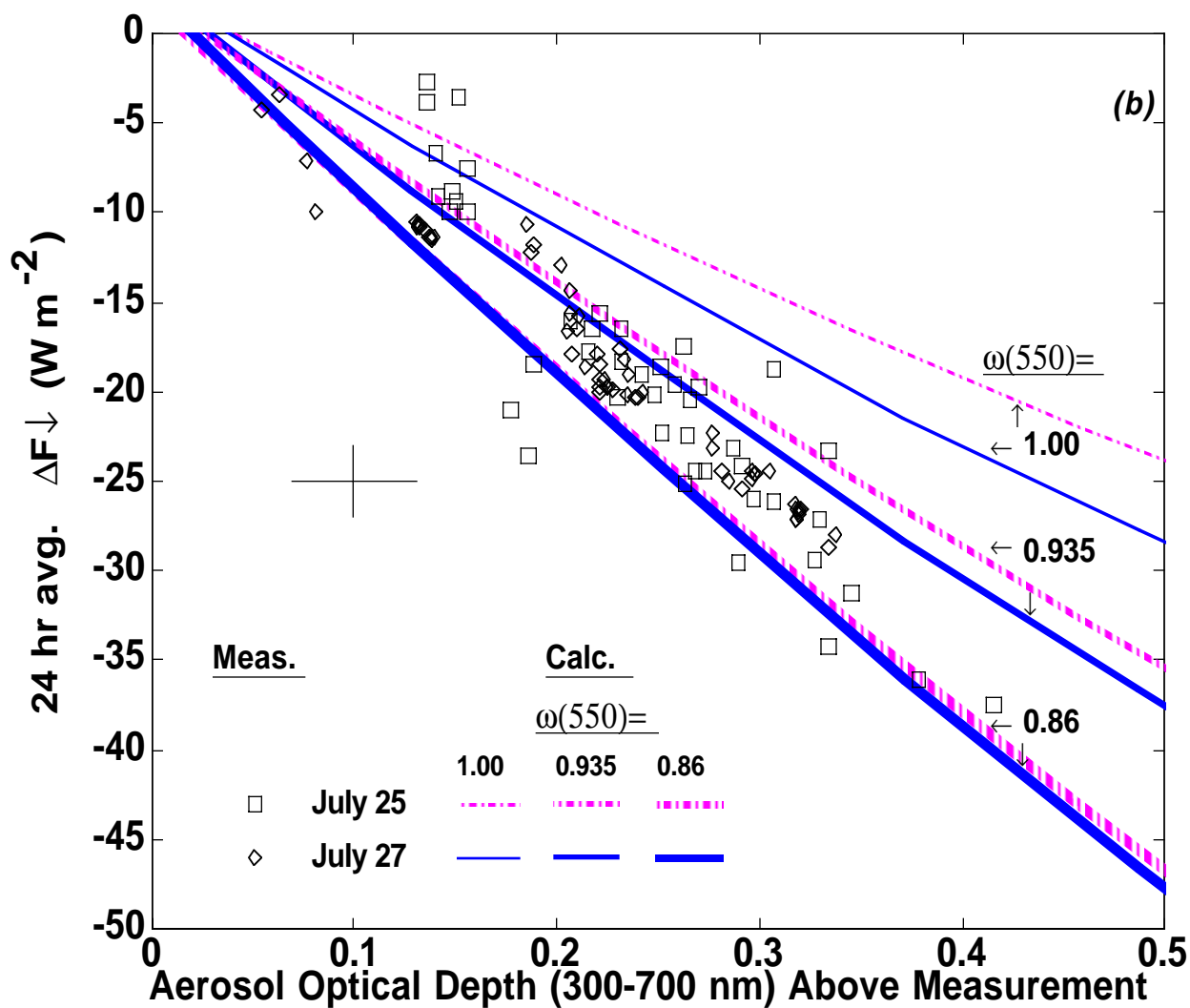
Figure 12. Comparison between aerosol-induced change in downwelling solar flux derived from C-130 pyranometer measurements (data points) and calculated (curves) for size distributions retrieved from sunphotometer optical depth spectra using an aqueous sulfate real refractive index and a range of imaginary indexes to give the ω (550) values shown. The error bar (cross) shows the uncertainty in flux change and broadband visible optical depth determined from the C-130 pyranometer measurements (Russell, et al., 1999b).